fluids

MDPI

Article

Frequency Specificity of Liquid-Fountain Swinging with Mist Generation: Effects of Ultrasonic Irradiation Angle

Xiaolu Wang and Katsumi Tsuchiya *

Department of Chemical Engineering and Materials Science, Doshisha University, Kyotanabe 610-0321, Kyoto, Japan
* Correspondence: ktsuchiy@mail.doshisha.ac.jp

Abstract: Atomization of liquid into the air attained through submerged ultrasound irradiation will involve the formation of liquid fountain, which exhibits a sequence of oscillating and/or intermittent characteristics/events: its vertical/*axial* growth and breakup; its *lateral* "compound swinging"; and its associated dynamics of mist formation and spreading. This study attempts to provide a mechanistic view of ultrasonic atomization (UsA) process in terms of the swinging periodicity of water fountain and to specifically examine the influence of ultrasonic irradiation (i.e., transducer installation) angle on the liquid-fountain oscillations with mist generated intermittently. Through high-speed visualization, it was qualitatively found that as the extent of tilt (from the vertical direction) in the irradiation angle was increased, the degree of occurrence of mist generation and the amount of identifiable mist being generated tended to decrease. This trend was associated with reductions in both the growth rate and breakup frequency of the fountain on the tilt. It was further found, through the analysis of time variation in the resulting angle of liquid-fountain inclination, that the swinging fountain fluctuated periodically in an *asymmetric* manner and its periodicity could be fairly predicted based on a proposed simple "pendulum" model. An optimum value of the transducer installation angle was observed and judged to be 2° from the viewpoint of effective mist generation as well as fluid dynamic stability of the UsA liquid fountain.

Keywords: ultrasonic atomization; liquid fountain/column/jet; fountain inclination; mist emergence; transducer setting angle; visual analysis

Citation: Wang, X.; Tsuchiya, K. Frequency Specificity of Liquid-Fountain Swinging with Mist Generation: Effects of Ultrasonic Irradiation Angle. *Fluids* **2022**, *7*, 306. https://doi.org/10.3390/fluids7090306

Academic Editors: Pengtao Yue and Mehrdad Massoudi

Received: 11 August 2022
Accepted: 9 September 2022
Published: 16 September 2022

1. Introduction

Ultrasonic atomization (UsA) techniques have been employed with an ultimate goal being a flexible green alternative for energy-efficient processes, including gas–liquid mass transfer enhancement/intensification [1,2], wastewater treatment [3,4], air purification [5–8], drug delivery [9,10], solvent–solute (or particles) separation [11–13], and/or its concentration [14,15].

Among those applications, a typical technique of installing the ultrasonic transducer is to set it, in the form of an oscillating disk, within a liquid and to irradiate ultrasonic wave almost vertically upward, but with a *slight tilt* [16,17]. In such a configuration, as the bulk liquid is irradiated at a high driving frequency (≈800 kHz or higher, [18]), a fountain of liquid will emerge from its free surface and micro- to nano-sized droplets could be generated—as mist—from the fountain.

If the installation angle/direction is exactly vertical, namely, the transducer's *flat* disk parallel to (or its angle being 0° vs.) the horizontal free surface, the acoustic fountain will be disturbed rather profoundly, either directly by relatively large drops of liquid separated from the fountain tip and then falling or indirectly by the associated undulation of the surrounding free surface, e.g., [19], which ideally should be avoided. The mist of droplets, on the other hand, have been investigated as mass-transfer or aerosol carriers by many researchers, in particular, regarding the effects of a variety of operating parameters on the

droplet size distribution (DSD), such as the driving frequency, oscillating-disk diameter, input power, liquid depth, liquid surface tension and viscosity, and the liquid-phase temperature, e.g., [11,20–23].

Whether tilted or not, the acoustic liquid fountain was proposed—based on a visualization study—to have a general configuration characterized by dynamics of the *four-region structure* consisting of (A) Foundation, (B) Bumpy-Surface, (C) Finely-Structured Surface and (D) Lumped-Crest Regions [19]. While such qualitative information needs to be clarified based on mechanistic support, it is quite a difficult task to reproduce or at least verify the fountain's dynamic structure over a diversity of the above-said operational parameters to be taken into account.

In regard to the mechanistic description of the fountain structure, the information available in the literature, e.g., [24–27] is mostly limited to a mere precursory structure or mound-like fountain. Xu et al. [24] conducted numerical simulation to realize the shape of the acoustic fountain with different ultrasonic parameters, through rigorous formulation of the theoretical bases. A notable finding is that the steady-attained height of acoustic fountain "step-increased with an increase in the acoustic pressure," with a step increment of half the ultrasound wavelength and the fountain surface tending to be stable over an "anti-resonant pressure" field. Kim et al. [25] experimentally investigated the mechanism controlling the stability of water protrusion; for better spatiotemporal resolution and control, particle image velocimetry (PIV) was applied to the induced flow field around the "ultrasonic *focal spot*," resulting from *focused* ultrasound at two distinct frequencies of ultrasound, 0.55 and 1.1 MHz. By varying the pressure level of the transducers, they observed three different regimes, namely, weak, intermediate (stable) and highly forced (explosive) fountains, with the detection of "the fountain height undergoing a stepwise change between the regimes" as reported by Xu et al. [24].

More specific experimental findings were reported by Aikawa and Kudo [26], including the relationship between thresholds for *free radical generation* and atomization under ultrasound irradiation, which should provide useful insights into the structural variation of dynamic fountains to be examined in the present study. The former is closely related to (or an outcome of) the *cavitation collapsing* process; the latter to the shape transition of free surface from a protuberance to a fountain of aspect ratio greater than unity. They detected the essentially *identical threshold* level in the increased transducer driving voltage—or equivalently, input power density (of 2.5 W/cm^2)—for all these four phenomena. Utilizing *focused* shadowgraphy, they further detected the *spotty-shaped high-intensity nodes*—created by the ultrasonic waves *incident on and reflected from* the "pressure-release" interface [28] of shape resembling a parabolic mirror; its convergence effect would promote the generation of cavitation bubbles inside the protuberance; the induction of cavitation promoted by such high-intensity nodes in turn could trigger the rapidly growing or "abruptly shape-transitioning" fountain that leads to the atomization.

When it comes to the structure and dynamics of acoustic fountains to be examined in this study, a typical fountain is no longer a mere protrusion, nor stable, and associated with mist spreading (out of the Finely-Structured Surface Region) as well as large drops and/or liquid ligaments formed as a result of tip breakup (the Lumped-Crest Region). Kawase et al. [29] and Yasuda et al. [30] used a 2.4-MHz ultrasonic transducer with installation angle of 5° at input powers of 20 and 18 W, respectively, to investigate the effects of carrier gas specifically and various operating conditions including the liquid properties on attaining efficient collection of UsA-concentrated alcohols. They provided a preferred flow mode of the carrier as well as some optimum conditions but no specific information regarding the fountain characteristics other than those of the mist as well as drops.

In this study, we apply high-speed imaging/image processing to observe/analyze detailed dynamics of the acoustic fountain by changing the angle of ultrasonic irradiation. The study involves mainly two objectives: to find an optimum irradiation angle, if it indeed exists, from the viewpoint of operability/stability of and effective mist generation out of the UsA fountain; and to quantify its periodicity both in the *axial* "growth-breakup" cycle and

lateral "swinging." The expected outcome of novelty lies in attempting to reveal factor(s) triggering mist emergence via experimental frequency analysis (fast Fourier transform) and theoretical prediction (pendulum model).

The paper is organized, after giving useful introductory literature information, as the experimental specifics on the system used, along with visual-image and time-series data analyses (Section 2); the resulting structural dynamics of the fountain both in the axial and lateral directions, followed by their frequency as well as time-series characterization, and modeling efforts—elaborated in the Appendix A—with its outcome in predicting the fountain-swinging periodicity (Section 3); and ends with itemized concluding remarks.

2. Experimental

The experimental setup used for visualizing the UsA process is shown in Figure 1. An ultrasonic transducer (Honda Electronics HM-2412, Toyohashi, Japan: 2.4 MHz) was placed on the bottom of a square vessel with its dimensions, 200 × 200 × 185 (height) mm. The transducer element (oscillating disk) itself was 20.0 mm in diameter, having an effective oscillating diameter of 16 mm. The installation or setting angle, θ_T, of the ultrasonic transducer was tested over the range 0–10° with a 1° increment. The input power applied to the transducer was changed over 7–13 W (input power density examined then ranged 3.5–6.5—or three specific values of 3.5, 5.0, and 6.5—W/cm^2, which is exclusively used in this study as an operating parameter).

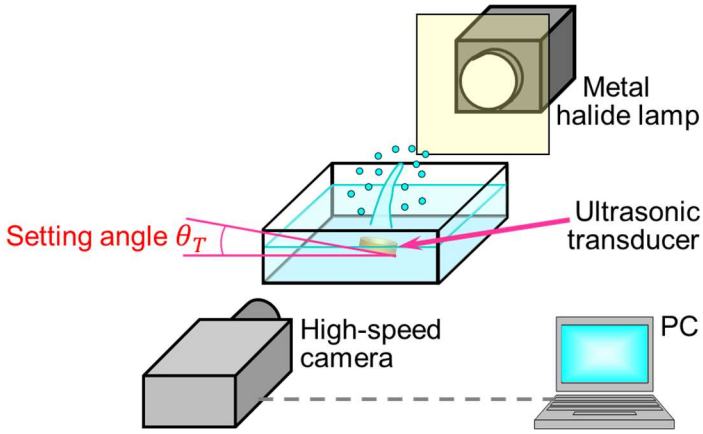

Figure 1. Schematic diagram of the experimental system for visual observation of ultrasonic atomization process for inclined liquid fountain.

The distance from the center of the oscillator to the free surface of the liquid (effective liquid depth) was kept 20 mm, or 27.5 mm above the vessel bottom. The liquid used was ion-exchanged water (Merck Millipore Elix® Essential UV3, Darmstadt, Germany); its temperature was adjusted, before each run, to 25 °C in a constant temperature bath. The liquid properties are presumed to be kept invariant during the UsA over a maximum 10-s period of operation.

2.1. High-Speed Visualization and Image Analysis

The visualization was carried out using a high-speed camera (REDLAKE MotionPro X4, Tokyo, Japan: frame rate(s) up to 5000 fps, with a resolution of at least 512 × 512 pixels, and an exposure time as short as 197 μs) under backlighting using a metal halide lamp (Lighterrace MID-25FC, Takatsuki, Japan). The imaging was started 5 s after the transducer was turned on, and a 1-s period of data was recorded. A sheet of light diffuser was installed between the liquid fountain and the lamp, thus reducing the non-uniformity of backlighting.

Figure 2 depicts—through a typical sequence of images—how two important "instantaneous" aspects of the liquid-fountain dynamics are determined visually: (1) the *axial* variations of its tip, confined by breakup and attained heights of the liquid fountain, and

(2) its *lateral* fluctuations characterized by the fountain swinging. Note that the very initial period of 0.6 ms or so covers the non-periodic startup growth phase, which should be excluded from the cyclic growth-and-breakup phase (see the 2nd to 5th frames covering one cycle). An image analysis software (DITECT Dipp Motion) was used to track the breakup and attained liquid heights; the vertical distance spanned over the period between the moment of fountain breakup and the succeeding one signifies the growth rate of the fountain, while the number of breakup events per unit time defines the breakup frequency.

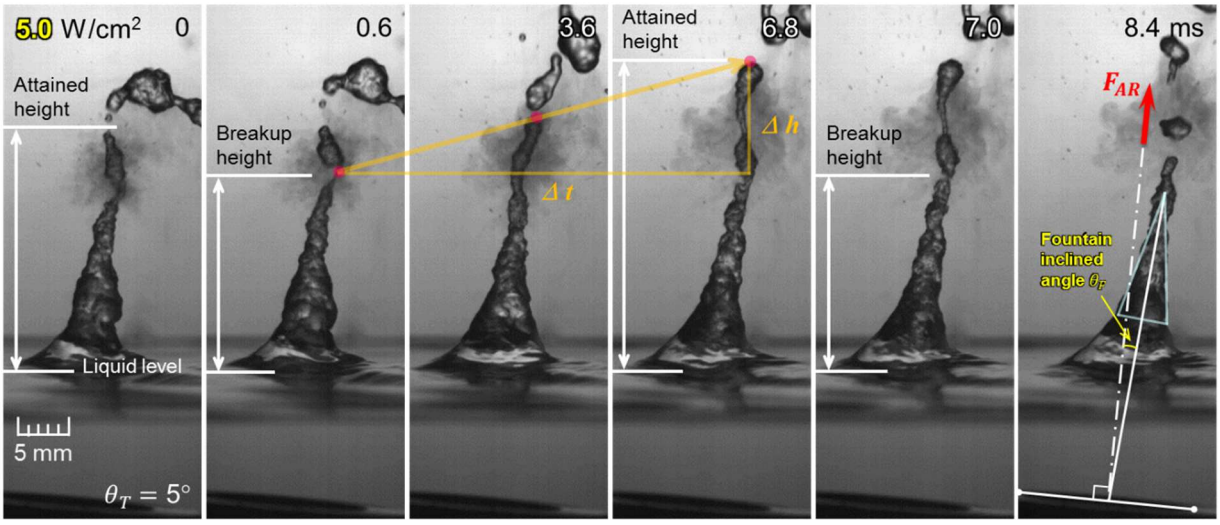

Figure 2. Time course of liquid-fountain dynamics signifying its axial variations, based on the defined fountain's breakup and attained heights; its lateral fluctuations are specified by θ_F (+ θ_T).

With the aid of a video analysis software (KEYENCE Movie Editor), the instantaneous state of swinging liquid fountain was specified in terms of its angle of inclination, θ_F, as depicted in Figure 2 (see the far right): first, the line perpendicular to the transducer disk (tilted by θ_T) is drawn, which is assigned to represent the "virtual axis" of the fountain emanating—acoustically radiating—from the center of the transducer; second, two tangential lines are drawn along the profile of the fountain surface to approximate the fountain outline as an equilateral triangle; the angle between the center line of the triangle and the virtual axis specifies the "net" inclined angle of fountain.

2.2. Time-Series Data Analysis

Once specified in its instantaneous state, or phase, the *lateral* dynamics of the acoustic fountain were analyzed in terms of time variation in its *inclined* angle $\theta_F = f(t)$. If the fountain exhibits a swinging motion, the resulting time-series data/signals $f(t)$ should contain periodic nature. Such data can be quantitatively processed based on the principle of frequency analysis. Since the current study aims to obtain the frequency characteristics—hopefully extracting the dominant frequency(ies) if any—the Fourier-transform analysis will be adopted; in its fast, discrete form of algorithm, fast Fourier transform (FFT), a given time-domain signal $f(t)$ is to be decomposed into a frequency-domain spectrum $F(\omega)$. In the FFT, the corresponding (to the former) sum of discrete elements, $f_{j+1}(t)$ ($j = 0, 1, \ldots, N-1$), sampled at equal intervals were processed through a fast, efficient algorithm (MathWorks MATLAB® 2019b) to obtain the corresponding (to the latter) spectrum:

$$F_{k+1}(\omega) = \sum_{j=0}^{N-1} \Psi^{jk} f_{j+1}(t) \quad (1)$$

where the term specifying the inner product on the right-hand side is given by the jk-th power of $\Psi = e^{-2\pi i/N}$ [31], and the thus-evaluated left-hand side provides the power spectrum, $|F(\omega)|^2$, which signifies the spectrum intensity at each frequency [18].

3. Results and Discussion

The effects of the angle (θ_T) of the ultrasonic irradiation, or transducer installation/setting, are presented below on dynamic (oscillating and/or intermittent) characteristics of the liquid fountain for the given input power densities; either axial or lateral direction will be prescribed to each characteristic under discussion.

It is noted here that the input power density may reflect the so-called *acoustic strength*, which could be a measure of acoustic *radiation pressure*/force—depicted schematically in Figure 2 (designated as F_{AR}, a sort of "tension" force trying to maintain the fountain straight along a given direction, presumably the transducer axis)—in a *traveling*-wave field or acoustic *streaming* in a *standing*-wave field [32–34]. These two competing factors would contribute to the liquid surface being pushed upwards, leading to the eventual formation of liquid fountain, e.g., [27]. It is also speculated that the more extensive these contributions are, the faster the fountain growth may be, and the greater the amount of resulting atomization would be.

3.1. Structure of Liquid Fountain with Mist

The images obtained of liquid fountain and/or some associated mist visible for different transducer setting angles $\theta_T = 0°$, 2°, 4°, 5°, 6°, and 7° at the applied power density of 5.0 W/cm^2 are shown in Figure 3. When the ultrasonic transducer is placed horizontally (0°), the fountain will be formed vertically along the direction of the transducer axis; individual small (visible) droplets along with the mist are observed to be scattered irregularly/intermittently (see Supplementary Material, Video S1) from the surface around the so-called Finely-Structured Surface Region (FSSR, [19,35]) mostly below the liquid fountain tip, or the Lumped-Crest Region (LCR). As the fountain ruptures vertically, the (large) separated tip drop—the remnant of the lumped crest—will not only disrupt the oscillation state of the fountain, often ending up merging with the remaining fountain, but also cause such disturbed fluctuations of the fountain surface to affect the direction of a higher part—including the FSSR as well as LCR—of the fountain in turn.

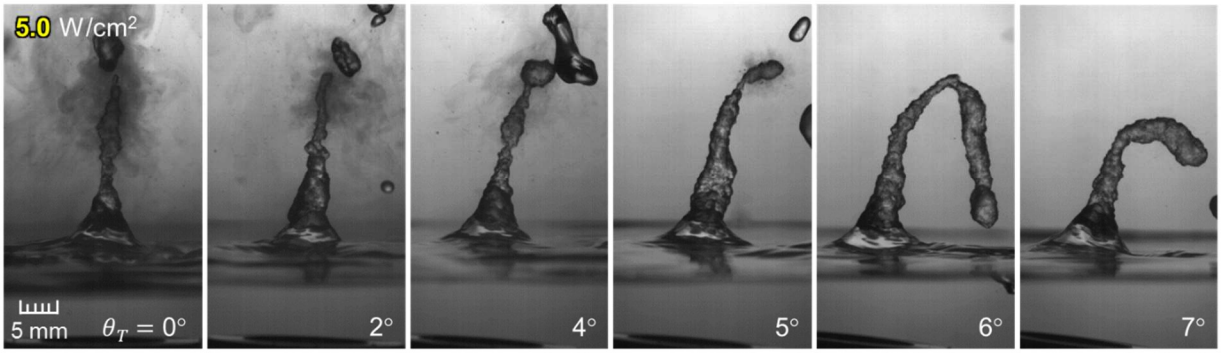

Figure 3. Images of liquid fountain obtained for different transducer setting angles at input power density of 5.0 W/cm^2.

With an increase in θ_T, the liquid fountain will be inclined correspondingly and may be bent in between—prior to reaching its tip—under the influence of gravity, while the axial interference from the separated drop(s) will be gradually reduced. In the range of θ_T increasing from 0° to 5°, the visually identifiable mist decreases gradually, but noticeably above 6°; and not identifiable/detected beyond 7°. The upper limit of θ_T in properly operating the UsA transducer is thus confined from the viewpoint of generating the mist.

3.2. Axial Growth and Breakup Dynamics of Liquid Fountain

The liquid fountain will repeat its dynamic phases between growth and breakup processes on a ms-time scale. Based on the image-analysis procedure described in Section 2.1, the breakup/attained heights, breakup frequency, and growth rate of the fountain were

determined for different input power densities. Three sets of data are provided under each condition to show the degree of reproducibility for each parameter.

Figure 4a shows the variations in the liquid-fountain breakup and attained heights for 3.5, 5.0, and 6.5 W/cm^2 with increasing transducer setting angle θ_T. Both the fountain heights increase with input power density. Over the range of θ_T examined, both the heights are regarded to be essentially invariant with the angle θ_T. As shown in Figure 4b,c, respectively, the breakup frequency and the growth rate of the fountain take maximum values at 2°; the former being clearly exhibited (by sharp peaks) but the latter being indicated by the moderate hills. Figure 4c, in particular, signifies the presence of a transition range (from 4° to 6°) that demarcates the high growth-rate range (0–4°) and the low-to-negligible range (6° or higher).

Notably, the appreciable reduction in the breakup frequency near $\theta_T = 0°$ ($\leq 1°$) could stem from the disruption of the oscillation "rhythm" of the fountain due to vertically interacting drops mentioned above; a slightly tilted transducer setting angle (0–3°) appears to have little impact on the fountain growth rate. Based on the image analysis, atomization is observed to occur both before and after the fountain breakup rather cyclically. It is sufficient to say here that the transducer installation angle should be set 2° in terms of effective mist generation and fluid dynamic stability of the liquid fountain.

3.3. Time-Dependent Characteristics of Fountain Swinging

The amplitude and frequency of fountain oscillations for two representative transducer setting angles, θ_T of 2° and 5°, were analyzed together with the amount of mist "determined" from the visual appearance on the relevant images such as the ones shown in Figure 3 (also see Supplementary Material, Videos S2 and S3).

Figure 5a shows, for the above two values of θ_T at 5.0 W/cm^2, time variations of the (net) fountain inclined angle θ_F along with the associated mist spreading detected. The position of red triangles in the figure specifies the moment (and the angle) of mist generation; the size of each triangle signifies the amount of atomization—judged to be either small or large, limited by the visual information only (see the inset images). While the fountain oscillations in θ_F are occasionally disrupted by tip-separated drops for $\theta_T = 2°$, the quasi-periodicity in the θ_F variation over time is still evident. Regarding the atomization, it is mostly triggered in cycle as the fountain inclined angle is shifted from positive to negative in the $0° \pm 5°$ range; particularly noticeable is multiple, sequential occurrence of misting (regarded as a single event) when the amplitude of oscillations in θ_F is larger. For the larger $\theta_T = 5°$, the fountain is no longer directly disturbed by the separated falling drops. In comparison to the smaller θ_T, the amplitude of θ_F oscillations, the angular range of triggering atomization, and more importantly/drastically, the degree of occurrence as well as the amount of atomization will all decrease. In addition, during one swing cycle, essentially only one-time mist generation can be detected.

The periodic (or at least quasi-cyclic) natures in the lateral and axial dynamics described above can here be contrasted more specifically in terms of their apparent frequencies. As shown in Figure 5b, selected portions of the fountain-swinging and growth–breakup time-series data would exhibit their own frequencies. The latter fluctuates more quickly than the former, with the frequency ratio of roughly 5 or greater—signifying the multiple (5–8 times) occurrence of axial growth and breakup in one lateral oscillation period. This frequency "gap" indicates that the fountain height could be regarded as effectively constant, averaged over one cycle of the fountain swinging. It should be noted here that even though the amplitude of oscillations in θ_F is appreciable during the swinging, the Foundation Region (FR) always formed in line with the direction of ultrasonic irradiation (see the inset t_3). Of particular importance, the heights of the FR and Bumpy-Surface Region (BSR) are essentially time-invariant (below the dashed line), and the occurrence of mist generation is mostly confined to the time-varying (but cyclic) FSSR. In this sense, the fountain swinging could be regarded as a motion of a dual-body (double-compound) pendulum with the FR as the pivoting region ([36,37]; to be discussed more extensively in Section 3.4).

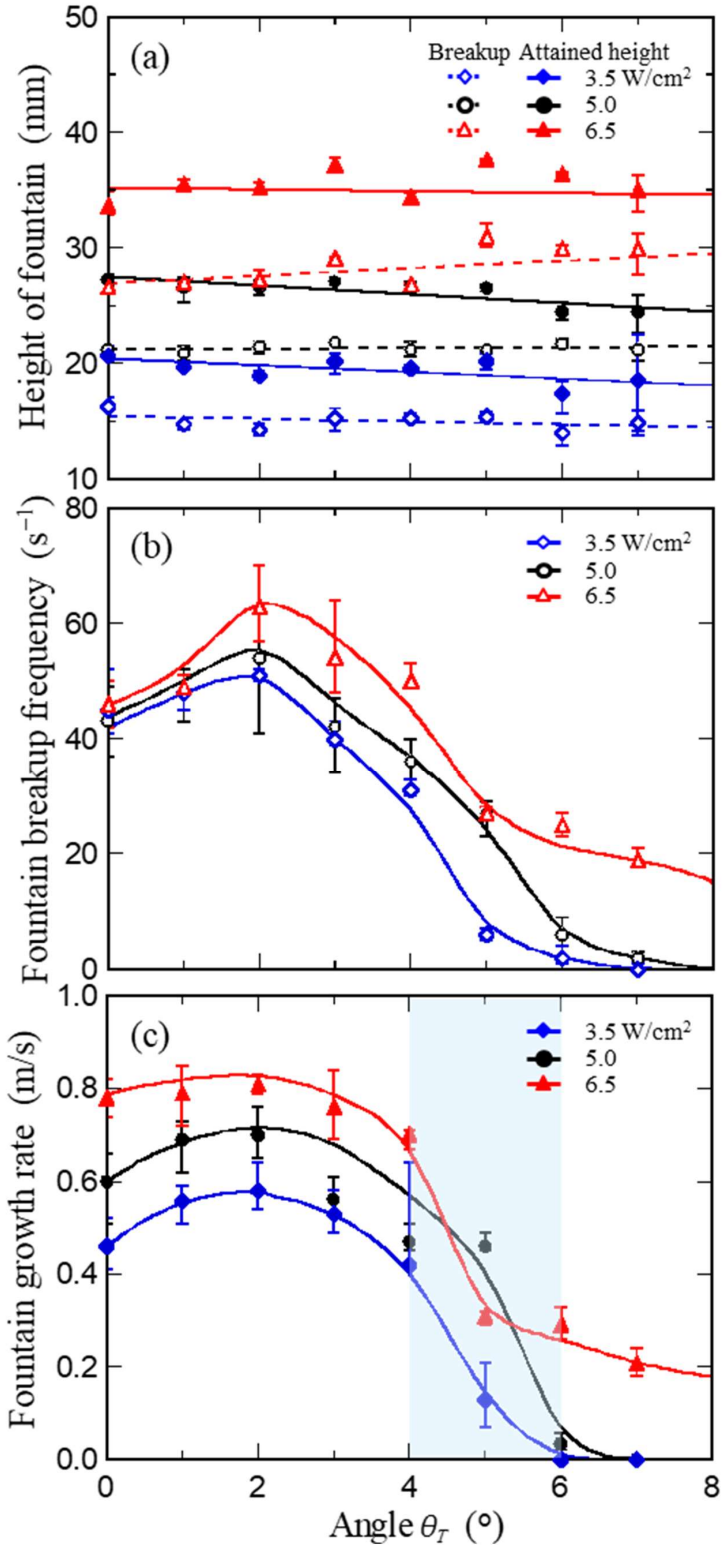

Figure 4. Effects of transducer setting angle on (**a**) breakup and attained heights, (**b**) breakup frequency, and (**c**) growth rate of liquid fountain for input power densities of 3.5, 5.0, and 6.5 W/cm^2.

Figure 6a,b shows the effects of the input power on the swinging characteristics at $\theta_T = 2^\circ$ and the corresponding FFT-analysis results, respectively. It is important to keep in mind that, on each time-series data given in Figure 6a, virtual/auxiliary data points (marked by small dots) are added, obtained via Lagrange interpolation; these points are necessary to perform FFT which requires equal intervals in the time coordinate. Some quasi-

periodicity in the variations of the fountain inclined angle over time is apparent for all the input power densities. With increasing input power density, the amplitude of oscillations in θ_F tends to decrease, while the degree of occurrence and amount of atomization do increase. The FFT analysis has revealed that—while quasi-periodic—the swinging fountain has a dominant frequency of 21, 21, and 24 Hz for 3.5, 5.0, and 6.5 W/cm^2, respectively. The same FFT analysis at $\theta_T = 5°$ for 5.0 W/cm^2 provides a dominant frequency of 18 Hz (not shown in the figure).

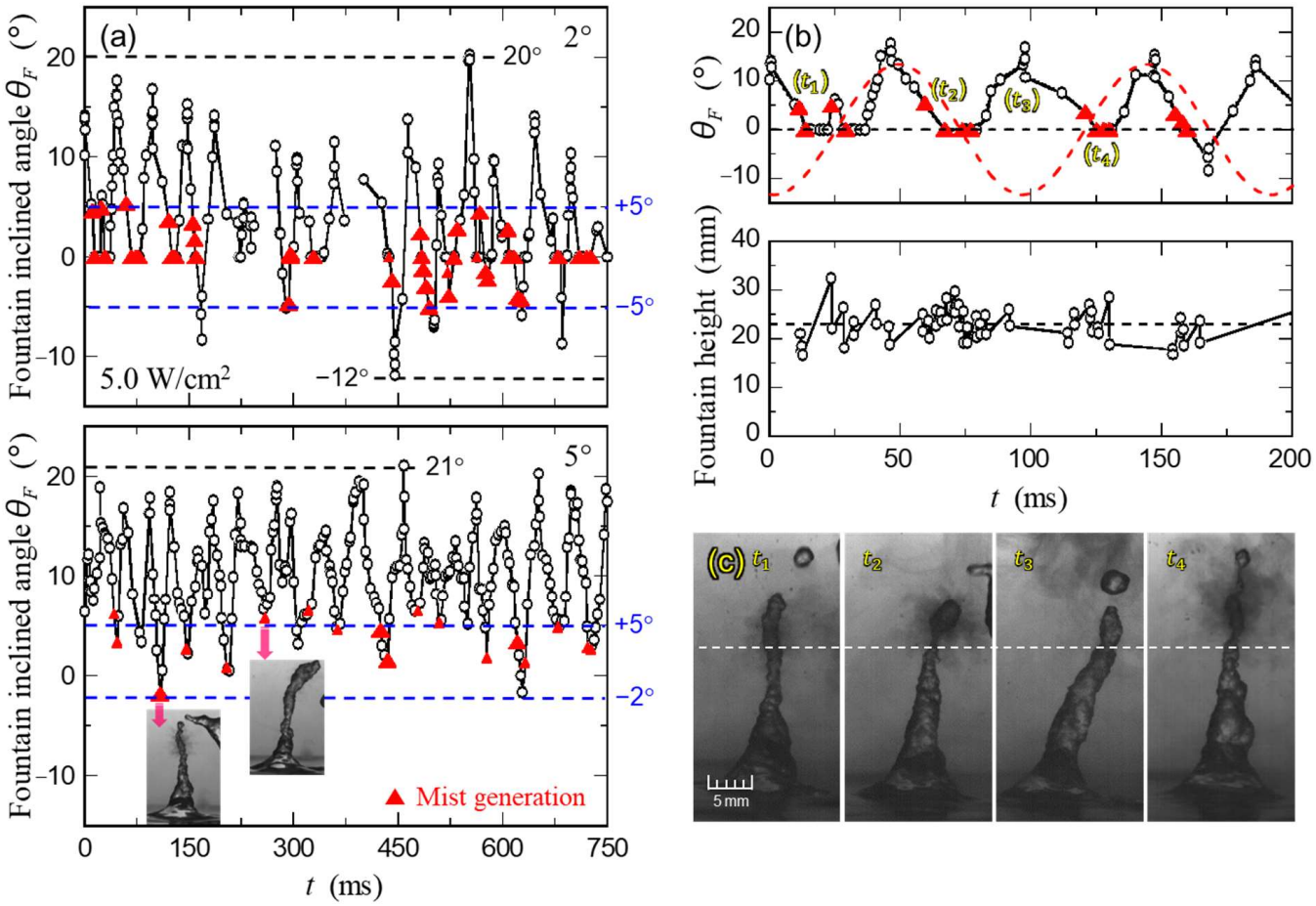

Figure 5. Time variations (**a**) in fountain inclined angle, associated with mist generation, for transducer setting angles θ_T of 2° and 5° at 5.0 W/cm^2, and (**b**) in fountain inclined angle and height for $\theta_T = 2°$ over selected time interval with (**c**) some images of fountain for representative phases of oscillations.

3.4. Model-Evaluated Periodicity of Fountain Swinging

As described in Sections 3.2 and 3.3, the acoustic liquid fountain will exhibit respectively quasi-periodic oscillations with recurring growth-and-breakup in the axial direction and swinging in the lateral direction—the latter, in particular, if the ultrasound is irradiated on the tilt—under the influence of gravity. The latter dynamics could then be regarded as a motion of a *planar* compound pendulum. In such phenomenological, intuitive modeling, a sequence of assumptions are needed for its mathematical formulation and predictive realization of the experimental findings described so far. The relevant details are provided in the Appendix A. A schematic configuration towards such modeling efforts is given in Figure 7.

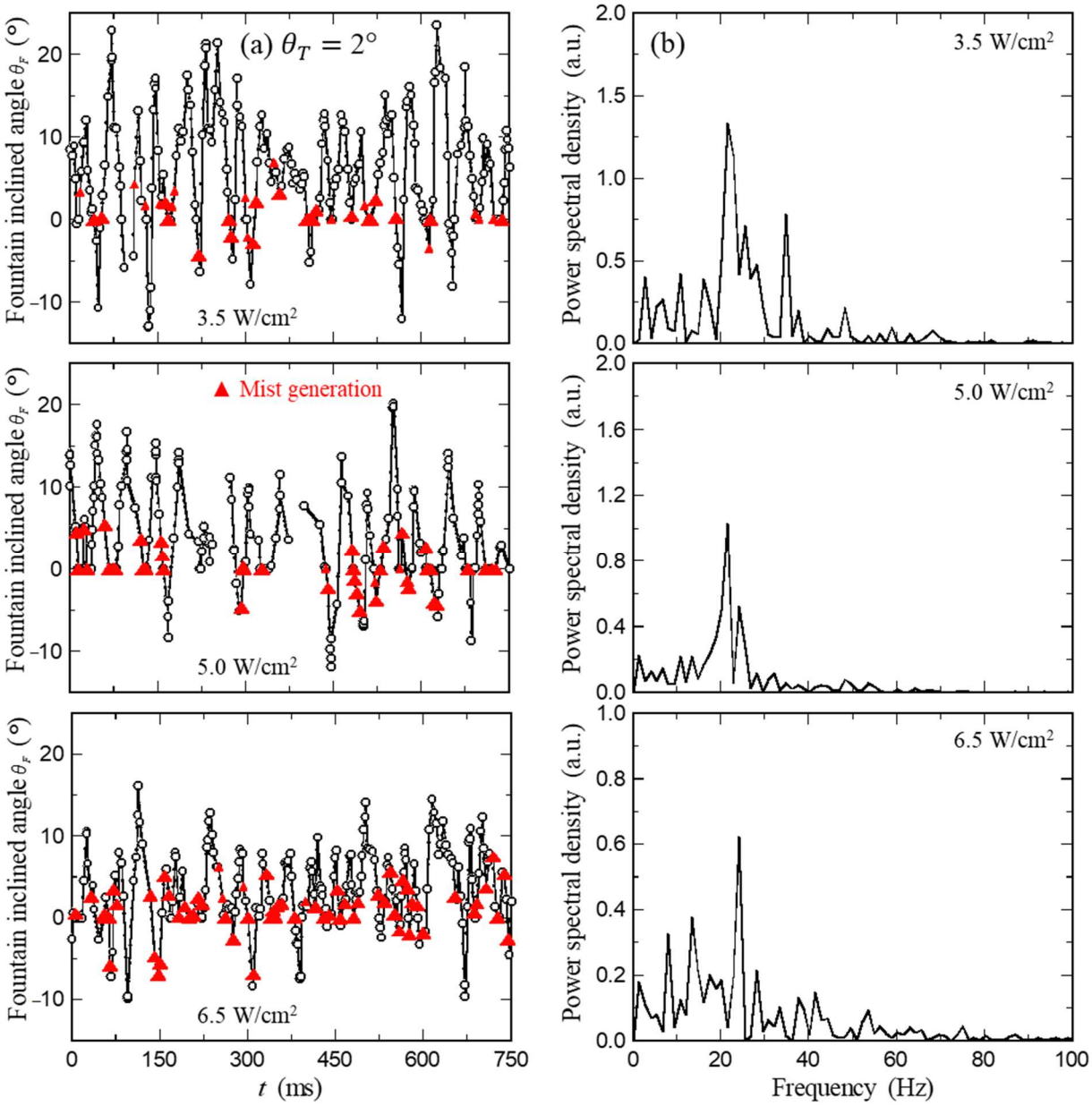

Figure 6. (**a**) Time variations in fountain inclined angle, associated with mist generation, for transducer setting angle of 2° at input power densities of 3.5, 5.0, and 6.5 W/cm^2, and (**b**) corresponding outcomes of FFT analysis for fluctuating inclined angle.

As elaborated on—and ending with the final simplification—in the Appendix A, the resulting model system of swinging fountain could be represented by a simple pendulum and would then be expressed mathematically as

$$I_F \frac{d^2\theta_F}{dt^2} + \left(F_{AR} L_F - m_F L_F^{\mathrm{CM}} g\right)\theta_F = m_F L_F^{\mathrm{CM}} g \theta_T \tag{2}$$

This is essentially a 2nd-order differential equation for a simple harmonic oscillation, which can be solved for the system angular frequency ω_F—with the *gravity-equilibrated* F_{AR} given by Equation (A2) and the *small-angle approximation* for θ_T, i.e., $\cos\theta_T \cong 1$—to yield the *natural frequency* of (harmonic) oscillation:

$$\omega_F^2 \equiv (2\pi f_F)^2 = \frac{m_F\left(L_F - L_F^{\mathrm{CM}}\right)g}{I_F} \tag{3}$$

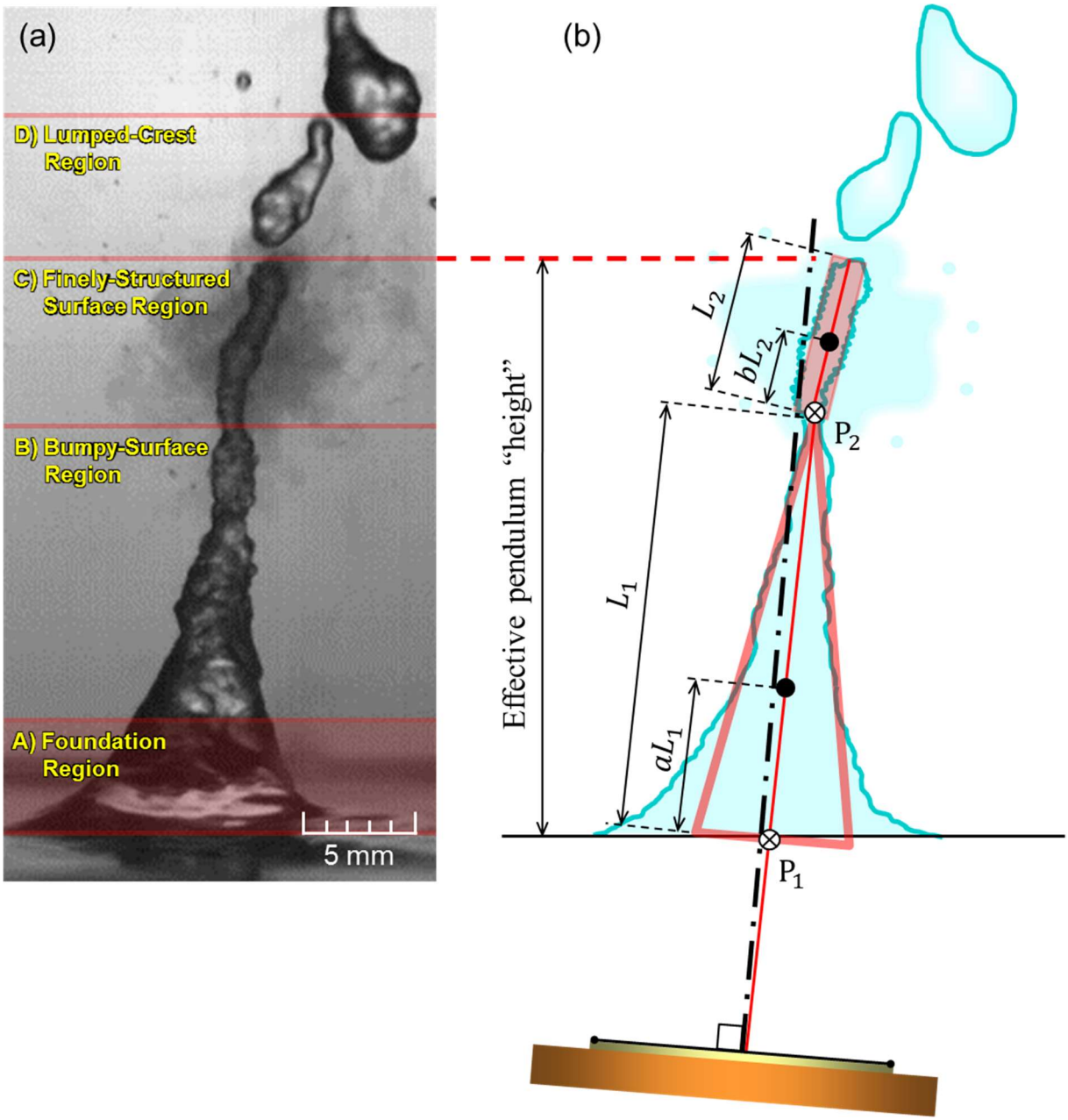

Figure 7. (**a**) General configuration of acoustic liquid fountain, proposed by Tsuchiya et al. [19], based on dynamics of *four-region structure* realized on typical fountain image, and (**b**) schematic representation of comprehensive definitions as well as specifications towards swinging fountain model.

which signifies the ratio of the torque imposed by gravity on the mass of the pendulum to the resistance to acceleration defined by the moment of inertia. The swinging frequency of the acoustic fountain in this study is then specified via Equation (A1) as

$$f_{\text{fount}} = 2f_{\text{pend}} \ (\equiv 2f_F) = \frac{1}{\pi}\sqrt{\frac{m_F\left(L_F - L_F^{\text{CM}}\right)g}{I_F}} \tag{4}$$

In this rather general expression, each parameter on the right-hand side could be provided as follows:

▷ The total mass moment of the fountain consisting of Bodies 1 and 2, the geometries of which are respectively a cone of the base radius R_1 and the height L_1, and a cylinder of the radius R_2 and the height L_2:

$$\begin{aligned} I_F = &\ I_1 + m_1(aL_1)^2 + I_2 + m_2(L_1 + bL_2)^2 \\ = &\ m_1\left(\tfrac{3}{10}R_1^2 + \tfrac{1}{9}L_1^2\right) + m_2\left(\tfrac{1}{2}R_2^2 + L_1^2 + L_1L_2 + \tfrac{1}{4}L_2^2\right) \end{aligned}$$

▷ The total mass itself of the fountain:

$$m_F = m_1 + m_2 = \rho_L \pi \left(\frac{1}{3}R_1^2 L_1 + R_2^2 L_2\right)$$

▷ The apparent center of mass for the fountain as a whole (L_F^{CM}) as well as the fountain length itself (L_F) combined as

$$L_F - L_F^{\mathrm{CM}} = \frac{m_1[(1-a)L_1 + L_2]g + m_2(1-b)L_2 g}{m_1 + m_2}$$

or

$$m_F\left(L_F - L_F^{\mathrm{CM}}\right) = \left(\frac{2}{3}L_1 + L_2\right)m_1 g + \frac{1}{2}L_2 m_2 g$$

Comparison(s) of the model-evaluated frequency $2f_F$ range, along with specific/representative values of the model parameters, determined based on the images obtained in this study, with the experimentally found (FFT-evaluated, dominant) frequencies, are summarized in Table 1. Reasonable agreement between these values appear to be obtained.

Table 1. Comparison of model-predicted and FFT-evaluated values for fountain-swinging frequency.

Input Power (W/cm^2)	L_1 (mm)	L_2 (mm)	R_1 (mm)	R_2 (mm)	$10^4 m_1$ (kg)	$10^5 m_2$ (kg)	$10^{10} I_1$ (kg m^2)	$10^{11} I_2$ (kg m^2)	Pred [Equation (4)] $2f_F$ (Hz)	Exp (FFT) Main Freq. (Hz)
3.5 @2°	10.8	4.8	2.9	0.8	0.95	0.96	2.4	0.31	19.1–21.5	21
5.0 @2°	16.6	5.2	3.5	1.0	2.10	1.60	7.7	0.81	16.2–17.9	21
5.0 @5°	14.7	6.2	3.1	0.7	1.50	0.95	4.3	0.23	18.4–19.0	18
6.5 @2°	18.5	8.2	3.0	1.0	1.70	2.60	4.6	1.30	13.4–17.3	24

As inferred from the above modeling outcome, the (asymmetric) fountain swinging observed in this study is of a resonant nature, i.e., occurring at or (if not completely undamped, or $\beta_i \neq 0$) near the natural frequency of the fountain as a whole. In dimensionless form, it can be expressed in terms of the resonance Strouhal number (Sr) based on the resonance frequency f_{fount} (or f_F in view of purely modeling perspective) together with some characteristic length and velocity. The latter two characteristics were selected in this study to be the basal diameter of the fountain, d_{base} ($= 2R_1$), and the propagation velocity of a capillary waveform [37] or the so-called capillary−inertial velocity [38] along the acoustic fountain surface. Such a specification will lead to the Strouhal number defined by

$$Sr_F = \frac{f_F\, d_{\mathrm{base}}}{\sqrt{2\sigma/\rho_l d_{\mathrm{base}}}} = \frac{f_F\, l_c}{\sqrt{2\sigma/\rho_l l_c}}\left(\frac{d_{\mathrm{base}}}{l_c}\right)^{\frac{3}{2}} \tag{5}$$

Note in this equation that the capillary length l_c defined by

$$l_c = \sqrt{\sigma/\rho_l g} \tag{6}$$

is explicitly introduced into the expression, along with the reduced basal diameter.

Further evaluation of the current model performance in providing the dominant frequency of the laterally oscillating liquid acoustic fountain in the air—besides comparing it with the FFT-evaluated values—was attempted in terms of thus-defined Strouhal number.

To do so, a well-accepted convention, in the multiphase fluid mechanics area, of plotting this dimensionless number against the Reynolds number (Re) was adopted in the present study; specifically utilized is a simple relationship/correlation proposed by Fan and Tsuchiya [37]—and well-supported by, e.g., Sankaranarayanan et al. [39]—given by the following form:

$$\frac{Sr}{Sr_0} = \left(1 - \frac{Ta_0}{Ta}\right)^2 \tag{7}$$

where Ta is the Tadaki number defined by $Ta \equiv Re\ Mo^{0.23}$ with $Re \equiv d_{\text{base}}\sqrt{2\sigma/\rho_l d_{\text{base}}}/(\mu_l/\rho_l)$—in this particular phenomenon of UsA fountain oscillations—and the Morton number which depends only on the liquid properties, $Mo \equiv \mu_l^4 g/(\sigma^3 \rho_l)$. The two correlative parameters, Sr_0 and Ta_0, are system-specific.

Figure 8 depicts, first, the present results for estimated values of the resonance Sr_F, obtained based on the above idealized model as well as the FFT-supported values of $Sr_{\text{fount}} = 2Sr_{\text{pend}}\ (\equiv 2Sr_F)$, each in four data points. To be compared with this liquid fountain "pendulum" is a single (gas) bubble associated with its wake—more specifically, the *primary wake* closely following the (zigzag) rising bubble in a stationary liquid—or their combined entity, "bubble−wake pendulum" exhibiting a similar oscillating/rocking motion [36,37]. The figure includes some selected data (seven) points along with the specifically "tuned" correlation—linear in the given coordinates—of such a gas (dispersed)−liquid system [37]. It should be noted that both the pendulum systems compare reasonably well with each other in terms of not only the linearly increasing trend but also the range of ordinate ($Ta\ Sr^{1/2}$) values—an encouraging outcome.

Additionally shown in Figure 8 are the acoustic liquid fountain consisting of a chain of beads/drops in contact, or the corrugated jet of liquid, studied specifically by Wang et al. [18], which exhibits characteristic oscillations in individual bead shapes; and fixed solid spheres exhibiting the surrounding fluid (gas or liquid) oscillations, known as vortex shedding behind the sphere (or in its wake), some data of which are selected from the compilation presented by Fan and Tsuchiya [37]. The former involves two modes of shape oscillations—assigned by n, the order corresponding to the representative shape of an oscillating drop (here, its vertical cross section being an ellipse: $n = 2$, and a diamond: $n = 4$; [18]). While not the same type of oscillations—*pendulum swinging* vs. *shape fluctuations*—their frequencies in terms of $Ta\ Sr^{1/2}$ demonstrate a similar range as well as trend. The latter essentially falls in the same range as well, despite—again—the different type of (*surrounding flow*) *oscillations*. The fact that all these comparisons (see Table 2 for a detailed list of the relevant data sets selected) apparently lead to the similar trend and range in the dimensionless frequency signifies that the relationship between Re and Sr, or more specifically, the linear relationship between Ta and $Ta\ Sr^{1/2}$, should provide quite a robust predictive scheme for a variety of *resonance* frequencies.

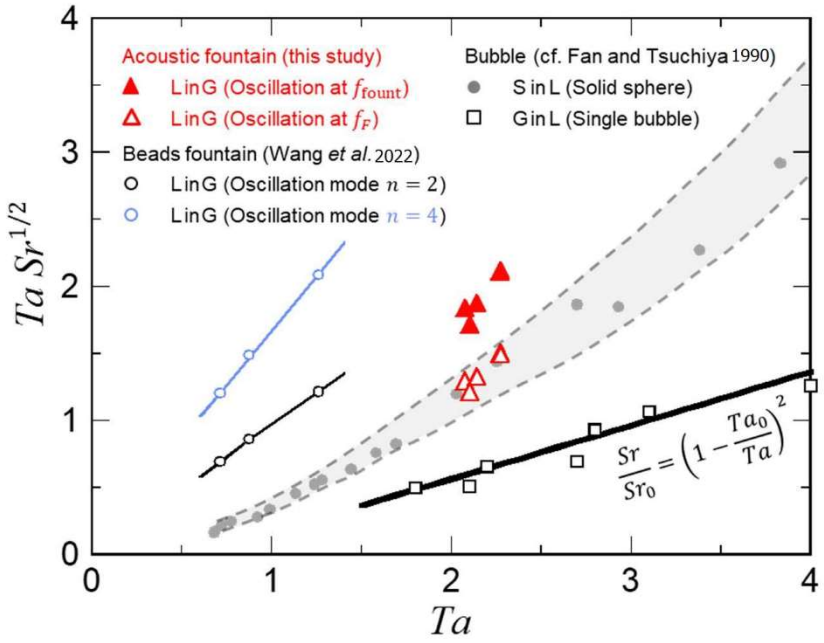

Figure 8. Resonance frequencies of various pendulum-like (or rocking), shape-deforming, and disturbed surrounding-flow oscillations represented by dimensionless form being correlatable via a simple expression proposed by Fan and Tsuchiya [37]; data adopted are from Wang et al. [18] for beads fountain and from Fan and Tsuchiya [37] for single dispersed entity.

Table 2. Comparison of model-predicted Strouhal numbers in different aspects of oscillating phenomena of UsA fountain.

Liquid fountain (W/cm^2)	d_{base} **(mm)**	f_{fount} **(Hz)**	f_F **(Hz)**	U_{capil} **(m/s)**	Re_{fount}	Sr_F	Sr_{fount}	Ta_{fount}	$Ta\ Sr_F^{1/2}$	$Ta\ Sr_{fount}^{1/2}$
3.5 @2°	2.9	21.5	10.7	0.16	1030	0.39	0.79	2.07	1.30	1.84
5.0 @2°	3.5	17.9	9.0	0.14	1130	0.44	0.87	2.27	1.50	2.12
5.0 @5°	3.1	19.0	9.5	0.15	1060	0.39	0.77	2.14	1.33	1.88
6.5 @2°	3.0	17.3	8.7	0.16	1040	0.34	0.67	2.10	1.22	1.72
Beads fountain (MHz)	d_{bead} **(mm)**	f_2 **(kHz)**	f_4 **(kHz)**	U_{capil} **(m/s)**	Re_{bead}	Sr_2	Sr_4	Ta_{bead}	$Ta\ Sr_2^{1/2}$	$Ta\ Sr_4^{1/2}$
1.0	1.47	0.13	0.38	0.21	114	0.92	2.68	1.28	1.22	2.09
2.0	0.74	0.36	1.08	0.29	81	0.91	2.72	0.91	0.86	1.49
3.0	0.49	0.66	1.99	0.36	66	0.90	2.70	0.74	0.70	1.21

4. Concluding Remarks

For ultrasound that is irradiated out of the transducer used with its installation angles ranging 0–6° or higher (up to 10° examined) and input power densities of 3.5–6.5 W/cm^2, the UsA fountain will exhibit a sequence of oscillating/intermittent features. Our main findings are summarized below:

(1) A slight tilt in irradiation of ultrasound should be advantageous in both operational and mist-generating performances. The acoustic liquid fountain will become improved in its operability/stability by avoiding the disruption of oscillation rhythm of the fountain from vertically interacting tip-separated drops;

(2) The atomization, or mist generation, is mostly—almost exclusively—triggered and enhanced as the *laterally* swinging fountain *comes across the direction of irradiation*, more specifically, with its inclined angle being shifted from positive to negative in the 0° ±

5° range. The degree of occurrence of mist generation and the amount of identifiable mist generated would decrease, associated with reductions in both the growth rate and breakup frequency of the fountain on the tilt;

(3) In line with such *axial* extents of growth and breakup of the fountain, both taking maximum values at the transducer installation angle of 2°, its optimum value should be recommended to be slightly tilted 2° from the viewpoint of stability of the UsA fountain and not to exceed 5° from that of effective mist generation;

(4) A mechanistic view of the UsA process is provided in terms of the swinging periodicity of liquid fountain with mist generated intermittently, in particular, if the ultrasound is irradiated on the tilt—under the influence of gravity. The periodicity of both the axial and lateral oscillations has been quantified—the latter in particular being model-predicted based on a simple *planar pendulum* concept proposed, partly confirmed via FFT-evaluated dominant frequency.

Supplementary Materials: The following supporting information can be downloaded at: https://www.mdpi.com/article/10.3390/fluids7090306/s1, Video S1: 0degSetting; Video S2: 2degSetting; Video S3: 5degSetting.

Author Contributions: X.W.: data curation, investigation, validation, writing—original draft preparation. K.T.: conceptualization, methodology, modeling, writing—original, reviewing, adding, and editing, supervision, project administration. All authors have read and agreed to the published version of the manuscript.

Funding: This research received no external funding.

Data Availability Statement: Besides the data available in this article, please contact the corresponding author for any additional data.

Acknowledgments: This work was supported in part by grants-in-aid from the Harris Science Research Institute of Doshisha University over the period of 2019−20FY; the first-year scholarship to X.W. is greatly appreciated.

Conflicts of Interest: The authors declare no conflict of interest.

Appendix A. Compound Pendulum Modeling

The first set of assumptions based on the visual information (see Figures 2 and 3) are listed as follows:

(1) The fountain, while altering its local shape dynamically, consists of two parts during the growth-and-breakup period, on average, simplified in geometry by a "cone" and cigar-shape or more simply a "cylinder." The former involves the FR and BSR, the latter the FSSR which accompanies mist spreading (Figure 2);

(2) This dual-part body as a single entity will be forced to maintain its axis straight along the tilted direction of θ_T —more stably if smaller than 4° (Figures 2 and 3, the fountain's equilibrium position *presumed*);

(3) When the tilting is increased beyond $\theta_T = 4$ or 5°, this single entity will experience its bending at the "connecting" region between the cone and the cylinder (Figure 3);

(4) Under the most probable complex situation, the fountain will behave as a two-body entity which exhibits two "separate" swinging motions with two pivotal regions—one near the base of the FR and the other around the connecting region—resembling the so-called "double compound" pendulum [40].

The second set of assumptions based on the time-series information (see Figures 5 and 6) can be proposed as follows:

(5) The waveform of fountain-swinging, exhibited in Figure 5b, particularly demonstrates the periodicity of the fountain's lateral dynamics with a peculiar nature of *asymmetricity* on the positive side of the angle θ_F. This experimental trend of *skewness*

signifies its frequency would be *twice* as high as an assumed symmetric (i.e., regular sinusoidal—given by the red, dashed smooth) waveform (cf. [41,42]);

(6) The axial growth−breakup time-series data, on the other hand, with frequencies as high as 5–8 times that of the lateral will lead to the assumed representation of time-invariant fountain height throughout the oscillations.

The third set of assumptions/simplifications would be needed for further idealization to mathematically express the prescribed pendulum system with realistic complexity reflecting the limited parametric information available, which could be added as follows:

(7) The "tension-like" force(s) required to sustain the pendulum straight in the direction of its axis on the equilibrium position—specified by a prescribed angle—should be the acoustic strength, or acoustic radiation pressure/force(s) (denoted by F_{AR}), which could be balanced by the gravitational contribution ($m_F g$) where m_F is the apparent mass of the pendulum (i.e., fountain) as a whole;

(8) The fountain, modeled by a dual-compound pendulum, is assigned to have the lower body of cone-shape of mass m_1 (Body 1, spanning the FR and BSR) and the upper body of cylindrical-shape of mass m_2 (Body 2, spanning the FSSR);

(9) The two bodies thus simplified geometrically will rotate about their specific pivotal locations—Bodies 1 and 2 around Pivots 1 and 2, respectively—where Pivot 2 serves as the joint connecting the two bodies.

All these assumptions are depicted in Figures 7 and A1 for more comprehensive definitions as well as specifications towards the intended mathematical formulation. In the following, essentially each assumption [out of ASM (1)–(9) with additional ones for further simplification] will be materialized into a series of model expressions/equations proposed—with the final expression for the model-evaluated frequency to be compared with the FFT-evaluated dominant frequency.

Visualized structure and dynamics "converted" into quantitative expressions (Figures 2, 3 and 7): The swinging fountain as a dual-part entity consists of one part rotating around the base center of the fountain FR (Pivot 1, P_1) with $\theta_F = \theta_{F1}$ (covering FR + BSR) and the other around the connecting region or point (Pivot 2, P_2) with $\theta_F = \theta_{F2}$ (FSSR), occasionally bent at Pivot 2 satisfying the relation $|\theta_{F1}| \leq |\theta_{F2}|$. The fountain will thus exhibit—as a double-compound pendulum—two separate (but mutually dependent/interactive) swinging motions characterized by the angular accelerations, $\frac{d^2\theta_{F1}}{dt^2}$ and $\frac{d^2\theta_{F2}}{dt^2}$, around Pivots 1 and 2, respectively [inferred from ASM (1), (3) and (4)].

Time-series characteristics "converted" into quantitative relationships (Figures 5–7): The axial fluctuations of the fountain, being regarded as time-invariant, would lead to its total length (tilted into the apparent height) which is a sum of individual parts, i.e., $L_F = L_1 + L_2 \neq f(t)$, while the lateral fluctuations are to be given by slower oscillations that are asymmetric in nature, specified as

$$f_{\text{fount}} = 2f_{\text{pend}} \equiv 2f_F \tag{A1}$$

[inferred from ASM (6) and (5), respectively].

Further simplifications "idealized" into model equations (Figure A1): The UsA fountain exerted by the "acoustic radiation" force(s), F_{AR}, *tries* by itself to maintain its "axial" direction "equilibrated" with the gravity component, i.e.,

$$F_{AR} = m_F g \cos\theta_T \tag{A2}$$

[inferred from ASM (2) and (7)]. As provided in the forces diagram (Figure A1) of the conceptual double-compound pendulum (Figure 7), this *axially equilibrated tension* force F_{AR} plays an important role in contributing as the *restoring* force, the extent of which could be expressed as

$$F_{ARi} \equiv (1 - \beta_i) F_{AR} \quad (i = 1,\ 2) \tag{A3}$$

for Bodies 1 and 2, respectively. Since these two contributions share the same direction as the fixed θ_T-directed tension F_{AR}, their instantaneous deviations—by θ_{F1} and θ_{F2}—from θ_T will cause the restoring effect as depicted in Figure A1. While such deviations should result in energy dissipation—assumed to be represented by some assigned factors β_i's—where $\beta_1 \leq \beta_2$ due to the above stated condition $|\theta_{F1}| \leq |\theta_{F2}|$, it would be boldly presumed in this study that both the factors be much smaller than unity—having the *small-angle assumption* (to be stated below)—leading altogether to $F_{AR1} \cong F_{AR2} \cong F_{AR}$.

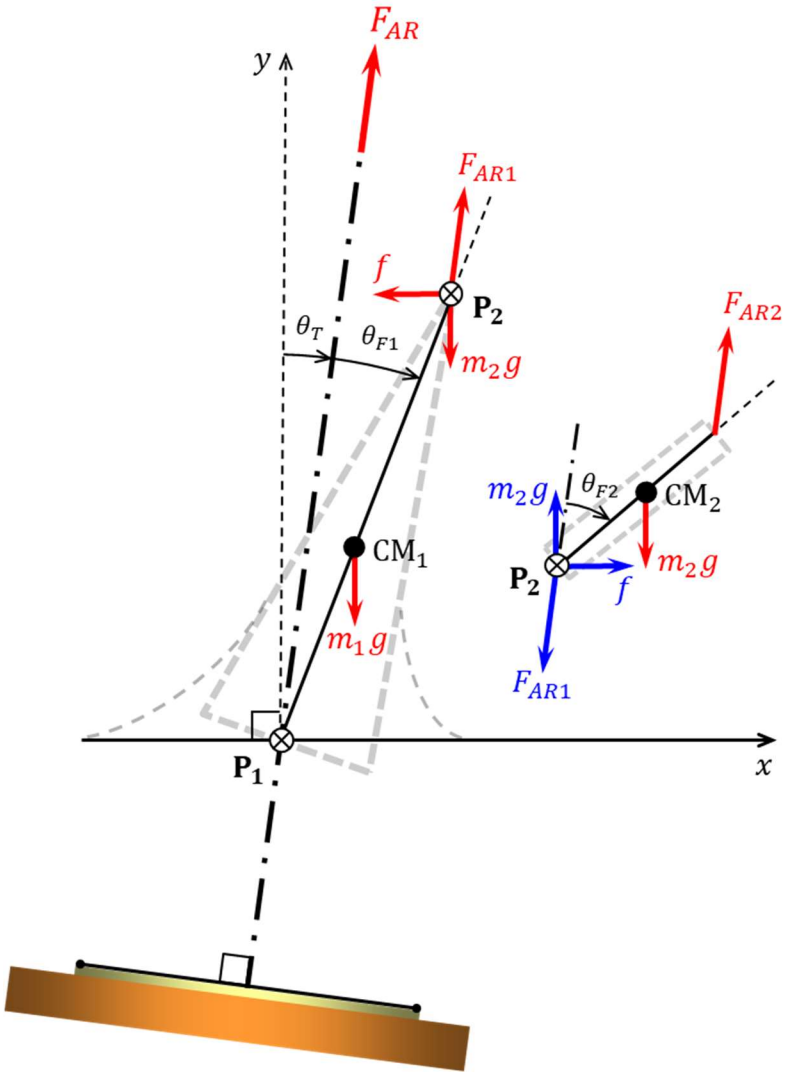

Figure A1. Forces diagram of conceptual double-compound pendulum inferred from modeled dual-part/body fountain depicted in Figure 7.

Based on the above series of simplifying arguments and the parameters specified in Figures 7 and A1, the balance in moments, or the angular equation of motion for θ_{F1}, about Pivot $\mathrm{P_1}$, can be expressed as

$$\begin{aligned} I_{F1}\frac{d^2\theta_{F1}}{dt^2} = &-F_{AR}L_1\sin\theta_{F1} \quad + m_1 g a L_1 \sin(\theta_{F1}+\theta_T) \\ &-fL_1\cos(\theta_{F1}+\theta_T) + m_2 g \;\; L_1\sin(\theta_{F1}+\theta_T) \end{aligned} \tag{A4}$$

Likewise, the balance in moments, i.e., the angular equation of motion for θ_{F2}, about (not Pivot P_2 but) the center of mass CM_2 yields

$$\begin{array}{rccc} I_2\frac{d^2\theta_{F2}}{dt^2} = & -F_{AR}(1-b)L_2\sin\theta_{F2} & +m_2gbL_2\sin(\theta_{F2}+\theta_T) \\ & -F_{AR} \qquad bL_2\sin\theta_{F2} & -fbL_2\cos(\theta_{F2}+\theta_T) \end{array} \tag{A5}$$

Here, the mass moments of inertia for the respective bodies (Bodies 1 and 2) around their respective centers of mass (CM_1 and CM_2)—I_1 and I_2—will be specified by assigning their respective body geometries/shapes [ASM (1) and (8)]. The corresponding mass moments of inertia around Pivots P_1 and P_2 will be given respectively by

$$I_{F1} = I_1 + m_1(aL_1)^2 \text{ and } I_{F2} = I_2 + m_2(bL_2)^2$$

The set of equations above, Equations (A4) and (A5), are to be rearranged—through the horizontal action−reaction pair of forces having the same magnitude f on the one hand—under the *small-angle approximation* of oscillations, i.e., $\sin\phi \cong \phi$ and $\cos\phi \cong 1$ with ϕ being θ_{F1}, θ_{F2}, $\theta_{F1}+\theta_T$ or $\theta_{F2}+\theta_T$ to get a corresponding set of linear(ized) 2nd-order differential equations:

$$\begin{array}{rcl} -f = & \frac{I_{F1}}{L_1}\frac{d^2\theta_{F1}}{dt^2} + F_{AR}\theta_{F1} - (am_1+m_2)g(\theta_{F1}+\theta_T) \\ = & \frac{I_2}{bL_2}\frac{d^2\theta_{F2}}{dt^2} + \frac{1}{b}F_{AR}\theta_{F2} - m_2g(\theta_{F2}+\theta_T) \end{array} \tag{A6}$$

The force f to be eliminated, on the other hand, can be specified by the horizontal acceleration at CM_2 (α_2) or its corresponding displacement (x_2) via Newton's second law [40]:

$$f = m_2\alpha_2 = m_2\frac{d^2x_2}{dt^2} = m_2\left(L_1\frac{d^2\theta_{F1}}{dt^2} + bL_2\frac{d^2\theta_{F2}}{dt^2}\right) \tag{A7}$$

Equations (A6) and (A7) are combined to remove f and, representing the 2nd derivatives in terms of the differential operator ($\mathbb{D} \equiv d/dt$) will yield the following coupled 2nd-order differential equations in a matrix form:

$$\begin{bmatrix} \left(\frac{I_{F1}}{L_1}+m_2L_1\right)\mathbb{D}^2 + [F_{AR}-(am_1+m_2)g] & m_2bL_2\mathbb{D}^2 \\ m_2L_1\mathbb{D}^2 & \frac{I_{F2}}{bL_2}\mathbb{D}^2 + \left(\frac{1}{b}F_{AR}-m_2g\right) \end{bmatrix} \begin{bmatrix} \theta_{F1} \\ \theta_{F2} \end{bmatrix} = \begin{bmatrix} (am_1+m_2)g \\ m_2g \end{bmatrix}\theta_T \tag{A8}$$

In the present study, this set of differential equations will not be attempted to be solved any further for two different oscillation angles, θ_{F1} and θ_{F2}; rather, another bold presumption would be made to have

$$\theta_{F1} \simeq \theta_{F2} \equiv \theta_F$$

where the dual-body pendulum would be reduced to a single-pendulum model.

References

1. Dong, Z.; Yao, C.; Zhang, X.; Xu, J.; Chen, G.; Zhao, Y.; Yuan, Q. A high-power ultrasonic microreactor and its application in gas–liquid mass transfer intensification. *Lab Chip* **2015**, *15*, 1145–1152. [CrossRef] [PubMed]
2. Tamidi, A.M.; Lau, K.K.; Khalit, S.H. A review of recent development in numerical simulation of ultrasonic-assisted gas-liquid mass transfer process. *Comput. Chem. Eng.* **2021**, *155*, 107498. [CrossRef]
3. Mahamuni, N.N.; Adewuyi, Y.G. Advanced oxidation processes (AOPs) involving ultrasound for waste water treatment: A review with emphasis on cost estimation. *Ultrason. Sonochem.* **2010**, *17*, 990–1003. [CrossRef] [PubMed]
4. Kunde, G.B.; Sehgal, B. Application of sol-gel assisted ultrasound-induced atomization in the mesostructuring of nickel aluminate UF membranes. *Microporous Mesoporous Mater.* **2021**, *325*, 111299. [CrossRef]
5. Tay, W.H.; Lau, K.K.; Shariff, A.M. High frequency ultrasonic-assisted CO_2 absorption in a high pressure water batch system. *Ultrason. Sonochem.* **2016**, *33*, 190–196. [CrossRef] [PubMed]
6. Tay, W.H.; Lau, K.K.; Shariff, A.M. High performance promoter-free CO_2 absorption using potassium carbonate solution in an ultrasonic irradiation system. *J. CO_2 Util.* **2017**, *21*, 383–394. [CrossRef]

7. Wei, J.; Gu, J.; Guo, J.; Li, W.; Wang, C.; Zhang, J. Simultaneous removal of nitrogen oxides and sulfur dioxide using ultrasonically atomized hydrogen peroxide. *Environ. Sci. Pollut. Res.* **2019**, *26*, 22351–22361. [CrossRef]
8. Marjanian, M.M.; Shahhosseini, S.; Ansari, A. Investigation of the ultrasound assisted CO_2 absorption using different absorbents. *Process Saf. Environ. Prot.* **2021**, *149*, 277–288. [CrossRef]
9. Dalmoro, A.; Barba, A.A.; d'Amore, M. Analysis of Size Correlations for Microdroplets Produced by Ultrasonic Atomization. *Sci. World J.* **2013**, *2013*, 482910. [CrossRef]
10. Kaur, J.; Singh, R.R.; Khan, E.; Kumar, A.; Joshi, A. Piperine-Loaded PLGA Nanoparticles as Cancer Drug Carriers. *ACS Appl. Nano Mater.* **2021**, *4*, 14197–14207. [CrossRef]
11. Nii, S.; Oka, N. Size-selective separation of submicron particles in suspensions with ultrasonic atomization. *Ultrason. Sonochem.* **2014**, *21*, 2032–2036. [CrossRef]
12. Kim, H.; Lee, J.; Won, Y.-Y. A simple derivation of the critical condition for the ultrasonic atomization of polymer solutions. *Ultrasonics* **2015**, *61*, 20–24. [CrossRef]
13. Hinman, J.G.; Hinman, J.J.; Janicek, B.E.; Huang, P.Y.; Suslick, K.S.; Murphy, C.J. Ultrasonic Nebulization for TEM Sample Preparation on Single-Layer Graphene Grids. *Nano Lett.* **2019**, *19*, 1938–1943. [CrossRef]
14. Kirpalani, D.M.; Suzuki, K. Ethanol enrichment from ethanol–water mixtures using high frequency ultrasonic atomization. *Ultrason. Sonochem.* **2011**, *18*, 1012–1017. [CrossRef]
15. Mai, N.L.; Koo, Y.-M.; Ha, S.H. Separation characteristics of hydrophilic ionic liquids from ionic liquids-water solution by ultrasonic atomization. *Ultrason. Sonochem.* **2019**, *53*, 187–191. [CrossRef]
16. Matsuura, K.; Kobayashi, M.; Hirotsune, M.; Sato, M.; Sasaki, H.; Shimizu, K. New separation technique under normal temperature and pressure using an ultrasonic atomization. *Jpn. Soc. Chem. Eng. Symp. Ser.* **1995**, *46*, 44–49.
17. Sato, M.; Matsuura, K.; Fujii, T. Ethanol separation from ethanol-water solution by ultrasonic atomization and its proposed mechanism based on parametric decay instability of capillary wave. *J. Chem. Phys.* **2001**, *114*, 2382–2386. [CrossRef]
18. Wang, X.; Mori, Y.; Tsuchiya, K. Periodicity in ultrasonic atomization involving beads-fountain oscillations and mist generation: Effects of driving frequency. *Ultrason. Sonochem.* **2022**, *86*, 105997. [CrossRef]
19. Tsuchiya, K.; Hayashi, H.; Fujiwara, K.; Matsuura, K. Visual analysis of ultrasonic atomization and its associated phenomena. *Earozoru Kenkyu* **2011**, *26*, 11–17. [CrossRef]
20. Kobara, H.; Tamiya, M.; Wakisaka, A.; Fukazu, T.; Matsuura, K. Relationship between the size of mist droplets and ethanol condensation efficiency at ultrasonic atomization on ethanol–water mixtures. *AIChE J.* **2010**, *56*, 810–814. [CrossRef]
21. Kudo, T.; Sekiguchi, K.; Sankoda, K.; Namiki, N.; Nii, S. Effect of ultrasonic frequency on size distributions of nanosized mist generated by ultrasonic atomization. *Ultrason. Sonochem.* **2017**, *37*, 16–22. [CrossRef]
22. Kooij, S.; Astefanei, A.; Corthals, G.L.; Bonn, D. Size distributions of droplets produced by ultrasonic nebulizers. *Sci. Rep.* **2019**, *9*, 6128. [CrossRef]
23. Panão, M. Ultrasonic Atomization: New Spray Characterization Approaches. *Fluids* **2022**, *7*, 29. [CrossRef]
24. Xu, Z.; Yasuda, K.; Liu, X. Simulation of the formation and characteristics of ultrasonic fountain. *Ultrason. Sonochem.* **2016**, *32*, 241–246. [CrossRef]
25. Kim, G.; Cheng, S.; Hong, L.; Kim, J.-T.; Li, K.C.; Chamorro, L.P. On the acoustic fountain types and flow induced with focused ultrasound. *J. Fluid Mech.* **2021**, *909*, R2. [CrossRef]
26. Aikawa, T.; Kudo, N. Relation between thresholds of free radical generation and atomization under ultrasound exposure. *Jpn. J. Appl. Phys.* **2021**, *60*, SDDD13. [CrossRef]
27. Orisaki, M.; Kajishima, T. Numerical analysis of water surface rising caused by underwater ultrasonic wave. *Trans. JSME* **2022**, *88*, 21-00377. [CrossRef]
28. Simon, J.C.; Sapozhnikov, O.A.; Khokhlova, V.A.; Crum, L.A.; Bailey, M.R. Ultrasonic atomization of liquids in drop-chain acoustic fountains. *J. Fluid Mech.* **2015**, *766*, 129–146. [CrossRef] [PubMed]
29. Kawase, Y.; Masuya, T.; Yasuda, K.; Nakamura, M. Effect of Flow Mode of Carrier Gas on Performance of Ultrasonic Atomization. *J. Chem. Eng. Jpn.* **2006**, *39*, 842–845. [CrossRef]
30. Yasuda, K.; Honma, H.; Xu, Z.; Asakura, Y.; Koda, S. Ultrasonic Atomization Amount for Different Frequencies. *Jpn. J. Appl. Phys.* **2011**, *50*, 07HE23. [CrossRef]
31. Percival, D.B.; Walden, A.T. *Wavelet Methods for Time Series Analysis*; Cambridge University Press: Cambridge, UK, 2000. [CrossRef]
32. Lee, J.; Yasui, K.; Tuziuti, T.; Kozuka, T.; Towata, A.; Iida, Y. Spatial Distribution Enhancement of Sonoluminescence Activity by Altering Sonication and Solution Conditions. *J. Phys. Chem. B* **2008**, *112*, 15333–15341. [CrossRef]
33. Lee, J.; Ashokkumar, M.; Yasui, K.; Tuziuti, T.; Kozuka, T.; Towata, A.; Iida, Y. Development and optimization of acoustic bubble structures at high frequencies. *Ultrason. Sonochem.* **2011**, *18*, 92–98. [CrossRef]
34. Son, Y.; Lim, M.; Ashokkumar, M.; Khim, J. Geometric Optimization of Sonoreactors for the Enhancement of Sonochemical Activity. *J. Phys. Chem. C* **2011**, *115*, 4096–4103. [CrossRef]
35. Fujita, K.; Tsuchiya, K. Cavitating Bubble inside Liquid Fountain of Beads Associated with Ultrasonic Atomization. In Proceedings of the 8th International Conference on Multiphase Flow 2013 (ICMF2013), Jeju, Korea, 26–31 May 2013. Paper 863.
36. Tsuchiya, K.; Fan, L.-S. Prediction of the wake size of a single gas bubble in liquid and/or liquid–solid media—The pendulum model. *Chem. Eng. Sci.* **1988**, *43*, 2893–2897. [CrossRef]

37. Fan, L.-S.; Tsuchiya, K. *Bubble Wake Dynamics in Liquids and Liquid–Solid Suspensions*; Butterworth–Heinemann: Stoneham, MA, USA, 1990.
38. Liu, F.; Ghigliotti, G.; Feng, J.J.; Chen, C.-H. Numerical simulations of self-propelled jumping upon drop coalescence on non-wetting surfaces. *J. Fluid Mech.* **2014**, *752*, 39–65. [CrossRef]
39. Sankaranarayanan, K.; Shan, X.; Kevrekidis, I.G.; Sundaresan, S. Analysis of drag and virtual mass forces in bubbly suspensions using an implicit formulation of the lattice Boltzmann method. *J. Fluid Mech.* **2002**, *452*, 61–96. [CrossRef]
40. Huat, O.J.; Ghista, D.N.; Beng, N.K.; John, T.C.C. Optimal stride frequency computed from the double-compound pendulum of the leg, and verified experimentally as the preferred stride frequency of jogging. *Int. J. Comput. Appl. Technol.* **2004**, *21*, 46–51. [CrossRef]
41. Alexander, R.M. *Principles of Animal Locomotion*; Princeton University Press: Princeton, NJ, USA, 2003. [CrossRef]
42. Van Bijlert, P.A.; van Soest, A.J.K.; Schulp, A.S. Natural Frequency Method: Estimating the preferred walking speed of *Tyrannosaurus rex* based on tail natural frequency. *R. Soc. Open Sci.* **2021**, *8*, 201441. [CrossRef]